ELSEVIER

Shear-induced structure in polymer–clay nanocomposite solutions

S. Lin-Gibson,[*,1] H. Kim,[2] G. Schmidt,[3] C.C. Han,[4] and E.K. Hobbie [*,1]

Polymers Division, National Institute of Standards and Technology, Gaithersburg, MD 20899-8543, USA

Abstract

The equilibrium structure and shear response of model polymer–clay nanocomposite gels are measured using X-ray scattering, light scattering, optical microscopy, and rheometry. The suspensions form physical gels via the "bridging" of neighboring colloidal clay platelets by the polymer, with reversible adsorption of polymer segments onto the clay surface providing a short-range attractive force. As the flow disrupts this transient network, coupling between composition and stress leads to the formation of a macroscopic domain pattern, while the clay platelets orient with their surface normal parallel to the direction of vorticity. We discuss the shear-induced structure, steady-shear rheology, and oscillatory-shear response of these dynamic networks, and we offer a physical explanation for the mesoscale shear response. In contrast to flow-induced "banding" transitions, no stress plateau is observed in the region where macroscopic phase separation occurs. The observed platelet orientation is different from that reported for polymer–melt clay nanocomposites, which we attribute to effects associated with macroscopic phase separation under shear flow.
© 2004 Elsevier Inc. All rights reserved.

1. Introduction

Polymer–clay nanocomposites have attracted significant interest because they exhibit synergistic behaviors derived from the two disparate components. Unique or enhanced mechanical, electrical, optical or thermal properties have been observed for both bulk and solution nanocomposites [1–11]. Such improvements in physical properties with the addition of nanoclay platelets are often influenced by the polymer–clay interaction and the state of dispersion or exfoliation. In general, good adhesion and favorable interactions between polymer and clay are necessary to achieve good exfoliation, which has in turn been found to be largely responsi-

ble for property enhancement. Furthermore, incorporating nanoscale platelets into a polymer matrix, as opposed to larger more conventional reinforcing agents, may also increase the light transmittance, allowing the preparation of transparent nanocomposite materials.

Poly(ethylene oxide) (PEO) and the synthetic hectorite clay Laponite (LRD) form viscoelastic solutions in water [12–14]. In equilibrium, adsorption of PEO segments onto the LRD surface [13] leads to the formation of a transient network or gel, and the diffuse polymer chains serve as a way of "bridging" neighboring clay particles, which feel a short-range electrostatic repulsion [13,15,16]. The quiescent or equilibrium structure is thus disordered or miscible in the sense that the suspensions are macroscopically homogeneous with ideal clay dispersion, or model clay exfoliation. Such PEO–LRD solutions are transparent and have good interfacial adhesion between the polymer and clay, and these characteristics are maintained in bulk materials to the extent that transparent nanocomposite gels can be prepared from well-dispersed polymer–clay solutions. From a practical point of view, this suggests the possibility of developing strong yet transparent films, coatings, and membranes with enhanced barrier properties associated with alignment of the clay nanoplatelets.

* Corresponding authors.
E-mail addresses: slgibson@nist.gov (S. Lin-Gibson), erik.hobbie@nist.gov (E.K. Hobbie).
[1] Official contribution of the National Institute of Standards and Technology; not subject to copyright in the United States.
[2] Present address: Department of Chemistry, Kyunghee University, Yongin, Kyungkido 449-701, Korea.
[3] Present address: Department of Chemistry, Louisiana State University, Baton Rouge, LA 70803, USA.
[4] Present address: Institute of Chemistry, The Chinese Academy of Sciences, Zongguancun, Beijing 100080, China.

As noted above, PEO–LRD suspensions can form physical gels via the dynamic adsorption–desorption of polymer segments onto the surface of the platelets, and these interactions greatly affect the viscoelastic properties and shear response of the mixtures, which in turn is relevant to the flow processing of clay nanocomposite melts and solutions. In the presence of polymer, the large aspect ratio of the clay may also lead to supramolecular organizations and structures under shear, reminiscent of other mesoscopic systems such as liquid crystalline polymers, surfactants, or block copolymers. The influence of shear on PEO–LRD solutions has been investigated via small-angle neutron scattering (SANS), from which the shear-induced anisotropy at the nanoscale can be determined [14]. Such measurements suggest that when subjected to sufficient shearing, the clay platelets orient with their surface normal along the vorticity direction. We have also used SANS measurements performed on contrast-matched samples and samples in pure D_2O to deduce the shear-induced orientation of the polymer with respect to the clay platelets. With increasing shear rate, the clay colloids orient first, with the polymer chains starting to stretch along the direction of flow at higher shear rates.

The goal of the present study is to further probe macroscopic changes in these solutions under shear using rheometry, light scattering, and optical light microscopy. Simultaneous shear light scattering and optical microscopy allow for a direct comparison of the morphological structure observed in both real and reciprocal space [17]. Here, we focus on the shear response of PEO–LRD mixtures in which the polymer content is fixed at 2% and the amount of clay is varied, as well as the 2% polymer–3% clay solutions of primary interest in our previous study [14]. The combination of SANS, light scattering, optical microscopy and rheometry provides a more complete physical picture of the shear response of these intriguing suspensions, which in turn offers a clearer understanding of the shear-induced mesoscale structures that can arise in response to the highly nonequilibrium conditions encountered during flow processing. Small and wide-angle X-ray scattering are used to fully characterize the equilibrium structure and extent of exfoliation of these physical polymer–clay gels.

2. Experimental

2.1. Materials

The synthetic hectorite type clay Laponite RD[5] (LRD) was obtained from Laporte Industries Ltd. The poly(ethylene-oxide) (PEO), with a molecular mass of 10^6 g/mol and a radius of gyration (R_g) of approximately 100 nm, was

obtained from Polysciences Inc. NaOH and NaCl were obtained from Aldrich. All reagents were used as received. The samples were prepared as described previously [14]. A stock solution was prepared by adjusting the pH and ionic strength of distilled, deionized water to 10 and 10^{-3}, respectively. PEO and LRD were then added to this solution in varying amounts. The samples were hand mixed for several minutes and centrifuged for 30 min each day over the course of several weeks. All samples were homogeneous, isotropic, and transparent prior to measurement. The various mixtures are denoted PEOx–LRDy, where x and y are the percent mass fraction of polymer and clay, respectively. Details of the SANS measurements and the corresponding data are described elsewhere [14]. These measurements were performed on the NG-7 30 m SANS instrument at the NIST Center for Neutron Research (NCNR) using a Couette flow cell. The geometry of shearing is in the $x–y$ plane, with flow along the x-axis, a constant velocity gradient along the y-axis, and vorticity along the z-axis. The SANS measurements probe structure over the interval $0.03 < q < 1.42$ nm^{-1}, where $q = 2\pi \sin(\theta/2)/\lambda$ is the scattered wave vector. Two different scattering geometries were used to procure measurements in both the $x–z$ and $y–z$ planes [14].

2.2. X-ray scattering measurements

Quiescent, time-resolved simultaneous synchrotron small-angle X-ray scattering and wide-angle X-ray diffraction measurements, SAXS/WAXD, were performed on the Advanced Polymers Beamline, X27C, at the National Synchrotron Light Source (NSLS), Brookhaven National Laboratory (BNL). The wavelength of the incident X-ray beam was $\lambda = 1.366$ Å, and the beam size was approximately 0.4 mm in diameter at the sample position. Synchrotron X-rays were collimated using a tapered tantalum pinhole collimator. The SAXS/WAXD profiles were recorded by two linear position sensitive detectors (European Molecular Biological Laboratory, EMBL), with sample-to-detector distances of 1788 mm for SAXS and 220 mm for WAXD. The SAXS scattering angle was calibrated with silver behenate and the intensity was normalized by incident beam fluctuations and calibrated with a LUPOLEN standard. The WAXD pixel resolution and the diffraction intensity were calibrated by comparing the synchrotron data with Siemens Hi-Star X-ray diffractometer data (Cu$K\alpha$) in $\theta–\theta$ reflection, and were corrected for detector nonlinearity and the empty beam scattering. The X-ray scattering measurements probe structures smaller than 60 nm.

2.3. Rheometry

Oscillatory-shear, steady-shear, and stress-relaxation measurements of the suspension rheology were performed on a Rheometric Scientific ARES instrument. Oscillatory-shear measurements were taken in a parallel plate configuration with 50 mm diameter plates, and steady-shear viscosity

and stress-relaxation measurements were performed in the same configuration using 25 mm diameter plates. A Rheometric SR-5000 instrument with a 40 mm cone-and-plate geometry was also used to measure the steady shear viscosity and the corresponding shear and normal stress. A fresh sample was used for each measurement. A pool of low viscosity silicon oil was used to seal the sample to avoid water evaporation. Duplicate measurements showed excellent reproducibility, with a relative standard uncertainty of less than 8%, where this corresponds to 2 standard deviations in the total experimental uncertainty.

2.4. Shear light scattering and optical light microscopy

The shear light-scattering photometer with optical light microscope was constructed at the National Institute of Standards and Technology [18]. The instrument provides real- and reciprocal-space measurements under steady shear over length-scales greater than 1 μm in the x–z (flow–vorticity) plane. The small-angle light-scattering detector and the microscope share the same mainframe. A simple translation switches the instrument from reciprocal-space to real-space mode. Samples were sheared in a parallel plate configuration with a 0.5 mm gap. A beam of light from a 15 mW He–Ne laser ($\lambda = 632.8$ nm) comes in from the top, and the scattered light is collected by two condensers and a thermo-electrically cooled CCD detector and is sent to a PC interface through an optical fiber. Due to the predominance of water in these suspensions, phase-contrast light microscopy was employed. This real-space imaging technique exploits the small difference in refractive index between the flow-induced structure and the surrounding solution. The projection of an incoherent light source through a phase ring focuses an annulus of the incident beam onto the phase plate of the microscope objective, which has a deposit on its annulus that retards the phase of the undiffracted beam and attenuates its intensity to the level of the diffracted beam, with the two recombining at the image plane to form the image. The magnification is such that the power spectrum of this image in reciprocal space can be compared directly with the light scattering pattern.

3. Results and discussion

3.1. Equilibrium structure and rheology

Over the range of polymer and clay compositions studied, equilibrium transitions from liquidlike to gellike behavior can be achieved by adjusting the clay and polymer content. In the current study, we examine the interaction of PEO and LRD in solution and how this influences the observed shear-induced structural changes. Small-angle X-ray scattering measurements were used to verify the dispersion of polymer and clay in water, as shown in Fig. 1a. As expected,
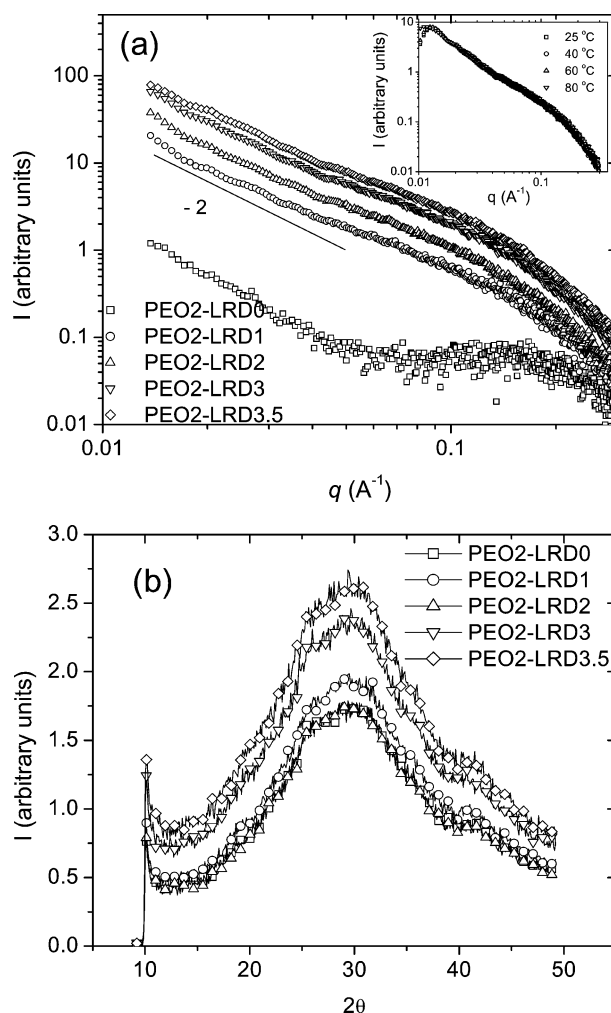

Fig. 1. (a) Small-angle X-ray scattering (SAXS) profiles of the quiescent solutions as a function of clay mass fraction, where the increase in low-angle intensity arises mostly from form-factor scattering. A high level of dispersion, or exfoliation, is inferred from the lack of the diffraction peaks usually observed in intercalated clay structures. (b) Wide-angle X-ray diffraction (WAXD) measurements as a function of clay loading, which shown only an amorphous peak characteristic of disordered systems.

the low-angle intensity increases with increasing clay content. The suspended clay scatters strongly at low q but the lack of additional peaks further confirms exfoliation. In addition, power-law dependence with a slope of approximately -2 was observed in the limit of low q, consistent with the form factor for disk-shaped 2D objects. The WAXD intensity is dominated by amorphous scattering and the patterns for solutions with and without clay are almost identical, as shown in Fig. 1b. The effect of temperature on the structure was also investigated (insert Fig. 1a), and little change was observed between 25 and 80 °C.

Rheological measurements on pure (2%) PEO, pure (3%) LRD, and a variety of PEO–LRD mixtures were used to assess the polymer–clay interaction and quantify the viscoelastic nature of the aqueous suspensions. Due to the anisotropy of the clay platelets, the structure and rheology of pure Laponite solutions are themselves quite complex, and these
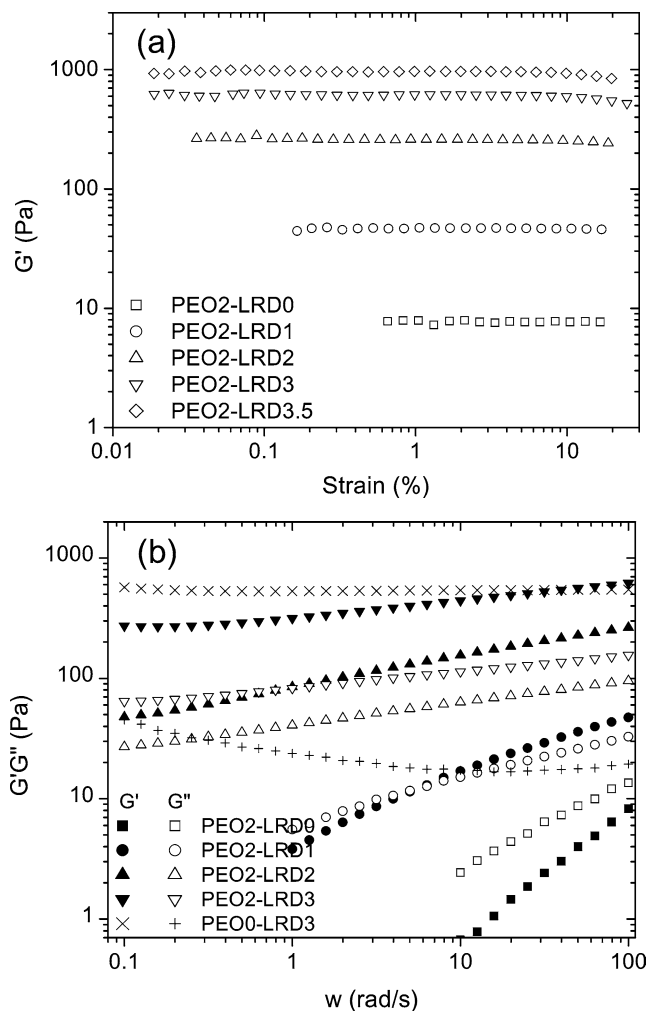
Fig. 2. (a) The storage modulus as a function of percent strain and clay loading for the polymer–clay solutions, which show linear-viscoelastic behavior over a broad range of strain. (b) The storage and loss modulus as a function of angular frequency and clay mass fraction, showing the evolution from shear-thinning fluid (PEO2–LRD0) and orientational glass (PEO0–LRD3) to physical gel (PEO2–LRD3).

topics have been the subject of previous research [15,19]. Even at concentrations as low as 1% clay by mass, the long-time annealed state appears to be an orientational gel or glass in which the platelets are not physically bonded to one another but their rotational freedom is frustrated by random packing [15,19].

Strain sweep experiments were first performed to determine the limiting strain (γ) for linear viscoelastic (LV) behavior, which showed an onset of nonlinearity at $\gamma = 3\%$, as shown in Fig. 2a. Oscillatory measurements were therefore performed at $\gamma = 2\%$, ensuring a LV response in the frequency-sweep experiments used to measure the complex shear modulus, $G^*(\omega) = G'(\omega) + iG''(\omega)$, where ω is the angular frequency. The real and imaginary parts of G^* (the storage and loss moduli, respectively) were measured for pure (2%) PEO, pure (3%) LRD, and PEO2–LRDy solutions with varied clay content, y, as shown in Fig. 2b. The characteristic time ($2\pi/\omega$) at which G' exceeds G'' is defined

as the terminal relaxation time. The pure 3% clay shows solidlike behavior, with G' being significantly larger than G'' and nearly independent of frequency over the probed range of frequencies. The pure PEO solution, on the other hand, shows a liquidlike response ($G'' > G'$), with a terminal relaxation time less than 0.06 s. Upon the addition of 1% clay (PEO2–LRD1), the terminal relaxation time becomes accessible to the experimental frequency window, suggesting that the addition of clay retards the longest relaxation of the PEO chains. Solutions with higher clay content did not show terminal relaxation at angular frequencies as low as 0.1 rad/s, corresponding to times longer than 60 min. The solidlike response of the samples becomes more pronounced with increasing clay content. A scaling exponent (n) is often used to characterize the power-law dependence of G' on ω. The exponent for PEO solutions without clay is 1.1, deviating significantly from the expected terminal value of 2, possibly due to polydispersity and/or entanglement effects. Since the response measured at low-ω is near the instrument's lower sensitivity limit, it is also possible that the terminal regime is simply not accessible. The scaling exponent of PEO2–LRD1 decreased to 0.95, but the response of this system is still essentially that of a viscoelastic liquid. The behavior of solutions containing 3% clay is strikingly different from those containing 1% clay. At a clay mass fraction of 3%, G' is enhanced with respect to the pure 3% clay at high frequencies, which we attribute to the formation of a transient network in which clay platelets are "bridged" by the PEO. The effective exponent n is 0.25 for PEO2–LRD2 and 0.06 for PEO2–LRD3.

The steady shear viscosity (η) and the shear stress (σ_{xy}) were also measured as a function of shear rate ($\dot{\gamma}$) and clay composition. For the pure LRD solution, applying steady shear reorients the platelets, and this yielding leads to a constant shear-thinning behavior, with $\eta \propto \dot{\gamma}^{-1}$ (Fig. 3a). By contrast, the pure PEO solution behaves like a shear-thinning viscous fluid, with a Newtonian plateau at low shear rates. The incorporation of LRD into the polymer solution increased the zero shear viscosity (η_0) and shifted the onset of shear thinning to lower shear rates. This trend continued with increasing clay content. At 2% polymer and 3% clay (PEO2–LRD3), a Newtonian plateau could not be observed at shear rates as low as 10^{-4} s^{-1}, and the system showed strong shear thinning behavior at low shear rates, similar to that of the pure clay solution. An excess viscosity with respect to the pure clay solution, however, is apparent at high shear rates. Fig. 3b shows an analogous plot of the shear stress, which does not show any plateau over the range of shear rates of interest. The first normal stress difference (N_1) for PEO2–LRD3 (Fig. 4) is negative at low shear rates, becoming positive above a critical shear rate of approximately 5-to-6 s^{-1}. Measurements of this quantity were not reproducible in samples of pure 3% clay in water and gave no detectable signal in samples of pure 2% PEO. The possible significance of a negative N_1 is discussed at the end of the paper.
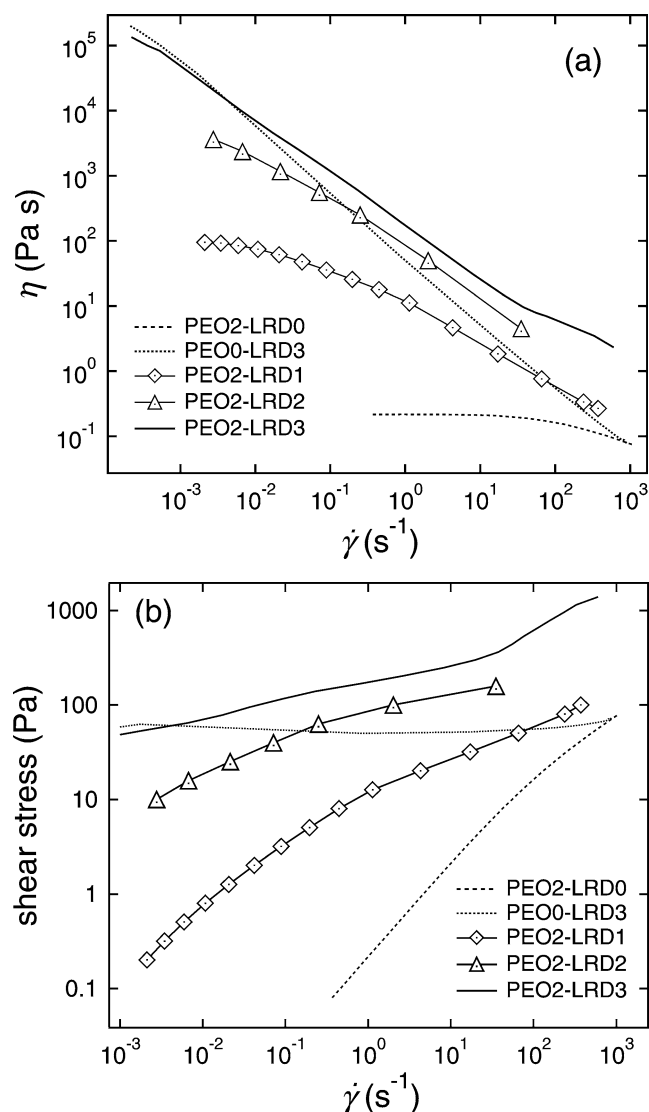
Fig. 3. (a) The steady-shear viscosity as a function of shear rate for a 2% polymer solution, a 3% clay solution, and polymer–clay solutions (2% polymer) at various clay concentrations (1, 2, and 3% by mass) at 25 °C. (b) Analogous plots of σ_{xy} vs shear rate do not show any stress plateaus.

One approach to better understand the interaction between the polymer and clay is to examine the step-strain relaxation spectrum, $G(t)$. A window that fully describes $G(t)$ can generally be obtained via shifting data collected at different temperatures with respect to a reference temperature using time–temperature superposition. To this end, we measured $G(t)$ at small γ between 20 °C and 75 °C, as shown in Fig. 5a. For all temperatures, the PEO2–LRD3 sample exhibits a short-time relaxation, followed by a nearly constant modulus G_0, which eventually relaxes fully at long times. However, an unexpected increase in G_0 was observed as the temperature increased, indicating that the gel strength increased with increased temperature, possibly due a stronger polymer–clay interaction. In addition, the relaxation time appears to increase with increasing temperature, also indicative of stronger associative interactions between the polymer
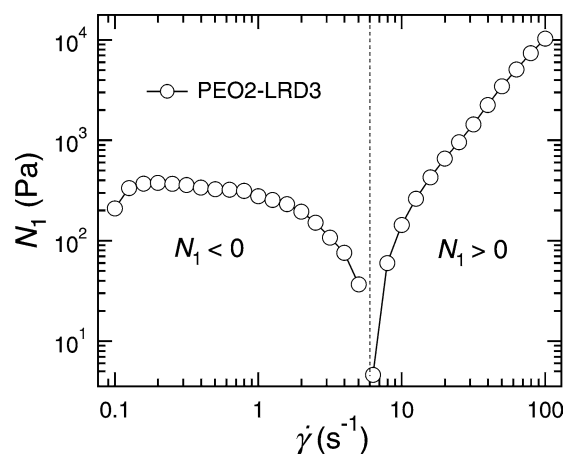

Fig. 4. The first normal stress difference, N_1, as a function of shear rate for a 2% polymer–3% clay solution (PEO2–LRD3) at 25 °C, with a reproducible transition from negative to positive N_1 at the indicated shear rate.

and clay. To verify this, both G' and G'' were measured at a single ω (1 rad/s) under a small γ (2%) as a function of temperature (Fig. 5b). Both G' and G'' increased with increasing temperature, in agreement with an enhanced gelation at higher temperatures. Since water becomes increasingly poor solvent for PEO as the temperature increases, it is also possible that the temperature increase may affect the bridging capability. If the adsorption of PEO segments onto the LRD surface is viewed within the context of the ether oxygens of the PEO—which act as a Lewis base—having a strong affinity for Bronsted acid sights on the LRD [13], then this temperature dependence might reflect an increase in the availability of these sights at higher T, although this question is open to further investigation.

3.2. Optical measurements of shear-induced structure

The rheological measurements suggest that the PEO2–LRD3 sample is particularly intriguing, as a dynamic network appears to form via polymer–clay adsorption–desorption. Our previous small-angle neutron scattering (SANS) measurements demonstrated the effect of shear on structure at the length scale of polymer and clay [14]. To gain a more complete understanding of the shear-induced structural transition, static light scattering coupled with optical light microscopy was used to probe PEO2–LRD3 nanocomposite solutions under shear. As mentioned above, a viscosity enhancement (with respect to pure PEO and pure LRD solutions) was observed for PEO2–LRD3 at high rates of shear. Optical turbidity measurements at $\lambda = 632.8$ nm (Fig. 6) suggest that this viscosity enhancement is accompanied by a shear-induced macrostructure, evident as a modest decrease in transmission with increasing shear rate. The absolute turbidity is $\ell^{-1} \ln(I_0/I)$, where ℓ is the gap thickness, I_0 is the initial intensity, and I the transmitted intensity. The turbidity decreases after reaching a maximum in the vicinity of 100 s^{-1}, suggesting dissolution of these domains above a threshold shear stress. We suggest that the macrodomains
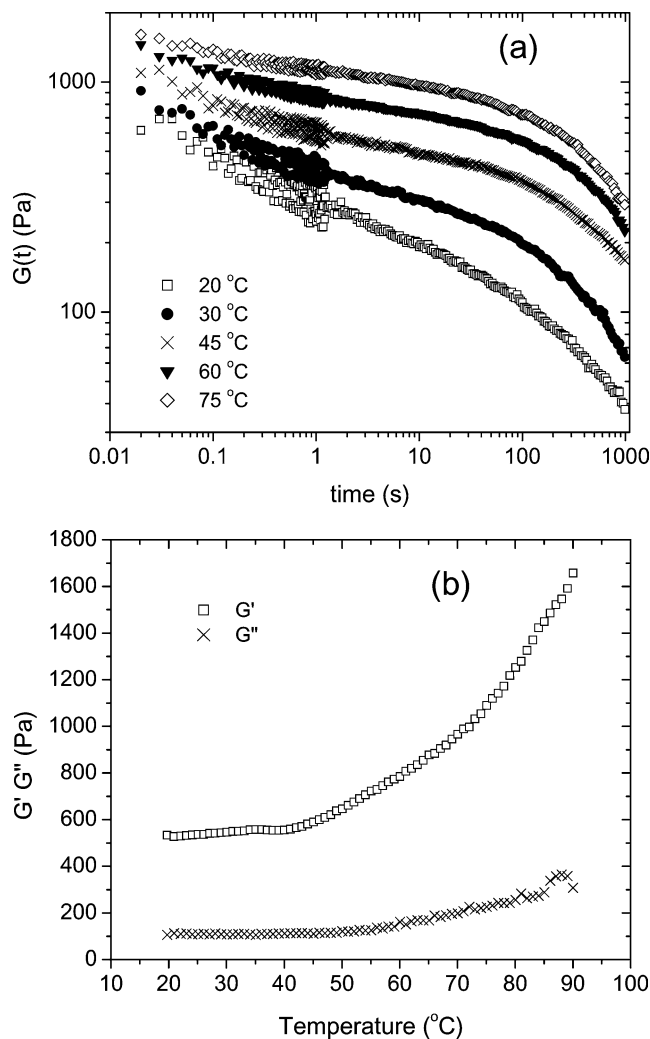
Fig. 6. The percent light transmission (at $\lambda = 632.8$ nm) and the absolute turbidity of PEO2–LRD3 as a function of shear rate, where the presence of macroscopic domains 1-to-10 μm in size is apparent as a decrease in transmission and an increase in turbidity above a critical shear rate of 5-to-10 s^{-1}. The appearance of these domains also coincides with the transition from negative to positive N_1 depicted in Fig. 4.
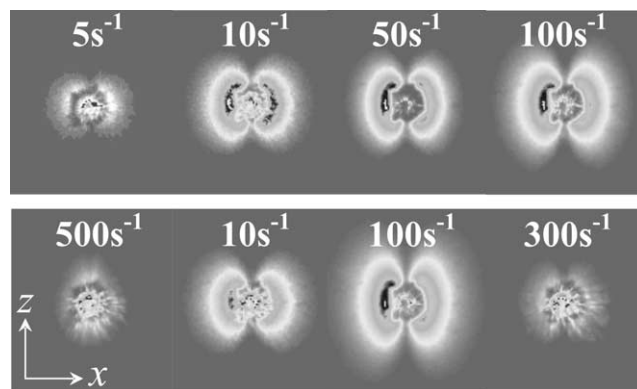
Fig. 7. Small-angle light scattering patterns for PEO2–LRD3 as a function of $\dot{\gamma}$, with the flow (x) and vorticity (z) directions as indicated. The width of each pattern subtends an angle of 27°. The domain pattern is first apparent at $\dot{\gamma} \approx 5$ s^{-1} and is strongest when the turbidity exhibits a maximum (50-to-100 s^{-1}), with the pattern disappearing at very high shear rates, where the sample is again transparent. As discussed in the text, the wing-like lobes reflect weak periodicity along the direction of flow in the spacing of vorticity-aligned "droplets". Analysis of simultaneously obtained real-space micrographs (Fig. 10) gives a mean domain size of around 5 μm, somewhat independent of $\dot{\gamma}$, with weak "liquid-like" order along the x-axis (Fig. 11).

Fig. 5. (a) Step-strain relaxation spectrum, $G(t)$, at temperatures between 20 and 75 °C. (b) Both G' and G'' at a single frequency ($\omega = 1$ rad/s) and small strain ($\gamma = 2\%$) as a function of temperature.

can be viewed as intact remnant "droplets" of the physical gel suspended in a surrounding fluid containing unassociated clay and polymer. The enhanced clay composition within the fragments, as well as orientation of platelets within these coherent structures, gives rise to the weak optical contrast between domain and solvent.

Small-angle light scattering patterns from PEO2–LRD3 measured in situ at various shear rates are shown in Fig. 7. Little or no scattering was observed at low shear rates, where the system is transparent and isotropic. A characteristic butterfly pattern starts to emerge at $\dot{\gamma} \approx 5$ s^{-1}, with the pattern being most pronounced for shear rates between 10 and 100 s^{-1}. The light-scattering pattern begins to deteriorate at higher shear rates, consistent with the measured decrease in turbidity shown in Fig. 6. The scattering is weak and nearly isotropic at both 300 and 500 s^{-1}, at which point lowering the shear rate causes the system to undergo rapid relaxation back to patterns previously observed at lower shear rates. The experiment was repeated several times on the same
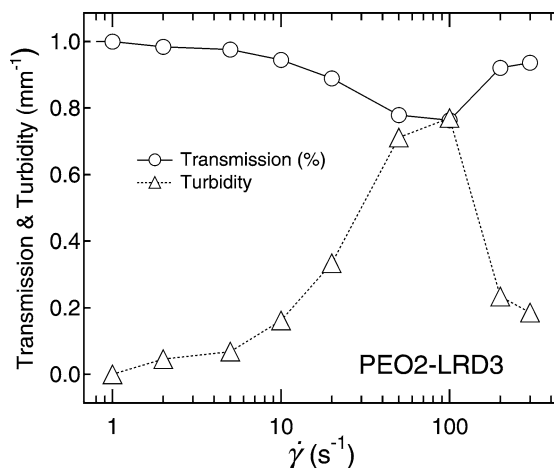
sample, and the response is reproducible. Samples of pure PEO (PEO2–LRD0) and pure LRD (PEO0–LRD3) showed no shear-induced optical structure that was discernable with light scattering and microscopy.

Fig. 8 shows projections of the patterns depicted in Fig. 7 along the flow (x) and vorticity (z) axes, where the two sets of data have been shifted by a factor of 5 and the incoherent background has not been removed. All of the scattering data can be well described by either a Gaussian or a Lorentzian in the low-q limit, or a squared-Lorentzian in the high-q limit, but no simple expression adequately describes the data over
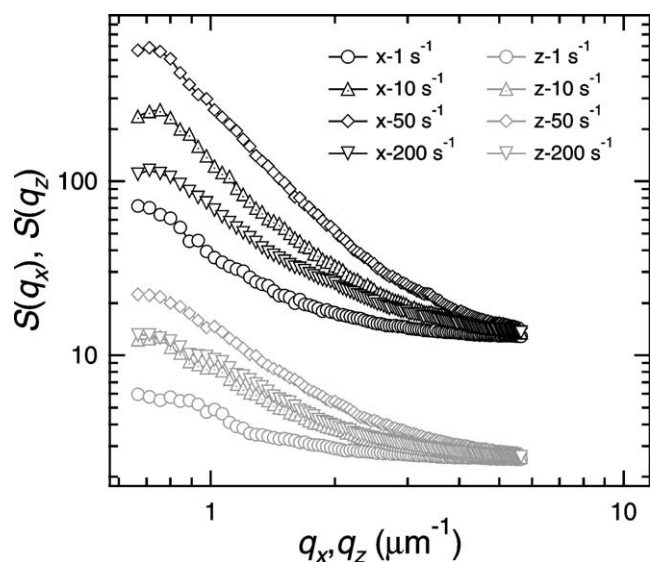
Fig. 8. Projections of the scattering intensity, $S(\mathbf{q})$, along the flow (x) and vorticity (z) axes as a function of shear rate for the data depicted in Fig. 5 (PEO2–LRD3). The scattering intensity along the x-axis has been multiplied by a factor of 5 for offset and clarity. The incoherent background has not been subtracted from these data.

Fig. 9. Optical micrographs of a PEO2–LRD3 suspension under steady shear flow, where the flow direction is to the right and the vorticity direction is vertical. The shear rate is indicated in the upper right corner, and the width of each micrograph is 150 μm.

the entire q-range, suggesting that the data might be well characterized by a linear superposition of these two trends. We have not pursued such an approach here, as it involves 5 free parameters over a limited range of q, and in our opinion thus offers limited physical insight. Equivalently, the background-corrected scattering data exhibit a qualitative crossover from q^{-2} behavior at low/intermediate-q to q^{-4} behavior at high-q, where the latter would appear to be consistent with sharp domain interfaces [17]. Somewhat more quantitatively, varying the background as a free parameter leads to power-law fits of the form q^{-D}, with D varying from around 2.5 at low-$\dot{\gamma}$ to 1.5 at high-$\dot{\gamma}$ along both $\hat{\mathbf{x}}$ and $\hat{\mathbf{z}}$. Such fits are restricted to less than 0.75 decades, however, and an interpretation in terms of "fractal" structures is thus not pursued here. Asymptotic fits to the expressions described above yield characteristic length scales, or correlation lengths, that depend only weakly on $\dot{\gamma}$ and suggest broad elongation of domains along the vorticity axis, with $\xi_z > \xi_x$. This anisotropy can be seen directly in the lobes of strong scattering evident in the 2D patterns. As discussed in more detail below, as well as in Ref. [20], these lobes reflect weak periodicity arising from enhanced domain–domain interactions along the direction of flow.

The butterfly scattering pattern has been observed for a variety of systems under shear. These include dilute polymer solutions, polymer blends and gels, but more directly relevant to the system under consideration, it has also recently been observed in polydimethylsiloxane fluids filled with colloidal silica, where it is attributed to the shear deformation of large colloidal aggregates arising from polymer bridging of the silica particles [21]. A similar-shear induced pattern has also recently been reported in thermoreversible gels of organophilic colloidal silica in hexadecane [22], where there
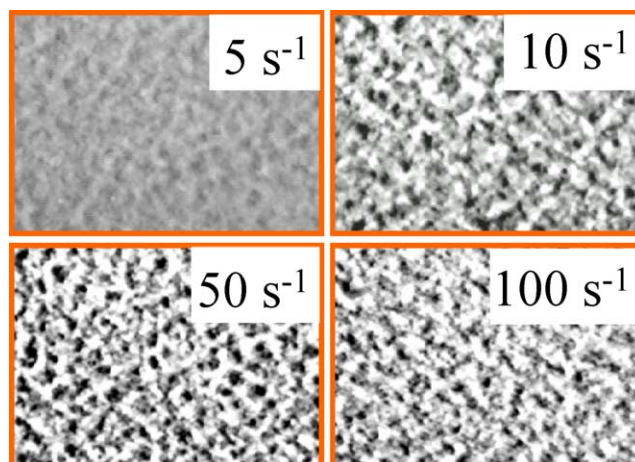
is no polymer bridging between colloidal particles. Patterns of this type have been attributed to the formation of large-scale structures due to increased spatial inhomogeneity and concentration fluctuation under shear, and the relation to "banding" in sheared complex fluids has been recently reviewed by Vermant [23]. We note that there are some striking similarities between the clay system we consider here and the colloidal structures described in Refs. [21–23], and we discuss this point in greater detail at the conclusion of the paper.

As in Ref. [21], the formation of shear-induced macrostructure observed in our polymer–clay system can be imaged directly using in situ real-space optical light microscopy, as shown in Fig. 9. These stroboscopic images are obtained simultaneously with the small-angle light scattering patterns. Like the light-scattering patterns, these images also suggest broad alignment along the vorticity axis, with a domain size that is somewhat independent of shear rate. Where the scattering and turbidity are weak, the contrast in the micrographs is weak, and where the scattering and turbidity are strong, this contrast is large.

The combined optical measurements of shear-induced macrostructure at $\dot{\gamma} = 100 \text{ s}^{-1}$ in the x–z plane are shown in Fig. 10. From ensembles of light microscopy images, we compute the two-point composition correlation function (Fig. 10b). This is calculated by first making the micrograph (Fig. 10c) into a binary image (Fig. 10d), which is used to compute $c(\mathbf{r}) = \langle \psi(\mathbf{r})\psi(0) \rangle$, where the field $\psi(\mathbf{r})$ denotes the local composition of macroscopic domains obtained from the optical light micrographs in a manner that is consistent with the measured turbidity [24], with $\psi = 1$ inside a domain (black regions) and $\psi = 0$ otherwise. The measured light scattering pattern, $S(\mathbf{q})$ (Fig. 10a), and the correlation function, $c(\mathbf{r})$, are related by a Fourier transform. At intermediate shear rates (10-to-100 s^{-1}) the domains exhibit broad elongation along the vorticity axis and weak
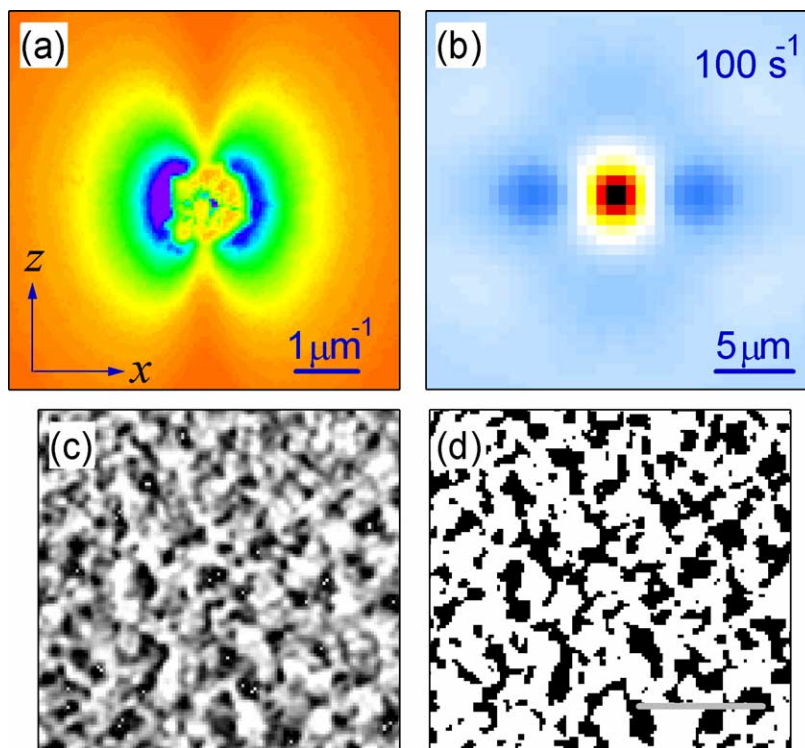
Fig. 10. Combined optical measurements of shear-induced macrostructure ($\dot{\gamma} = 100$ s^{-1}, PEO2–LRD3) in the x–z plane. Image (a) is the small-angle light-scattering pattern, $S(\mathbf{q})$. Image (c) is a corresponding real-space micrograph, which yields a map (d) (scale bar = 25 µm) of $\psi(\mathbf{r})$, the local composition of gellike domains. Image (b) is the two-point composition correlation function, $c(\mathbf{r})$, computed from $\psi(\mathbf{r})$.
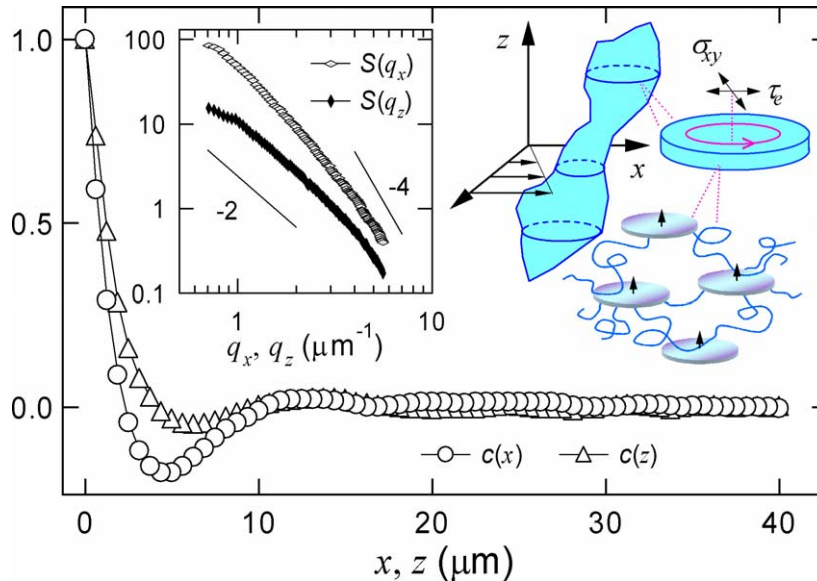

Fig. 11. The figure shows projections of $c(\mathbf{r})$ along the flow (x) and vorticity (z) directions, and the inset shows analogous projections of $S(\mathbf{q})$, where the incoherent background has been subtracted from the measured intensity. The cartoon depicts how biaxial internal stresses might orient the platelets in the manner suggested by previous SANS measurements on identical suspensions.

periodicity along the flow direction, as evidenced by well-defined correlation holes in $c(\mathbf{r})$ (the real-space analog of the wing-like lobes of strong scattering in $S(\mathbf{q})$), which appear as a well-defined correlation minimum in $c(x)$ shown in Fig. 11. The correlation lengths ξ_x and ξ_z characterizing the spatial coherence of the domain pattern can be obtained

by fitting projections to $c(x_i) \approx \exp(-2x_i/\xi_i)$ in the $x_i \rightarrow 0$ limit, where these projections are shown in Fig. 11. This is equivalent to the squared-Lorentzian fit of the scattering data in the high-q limit described above [20]. The mean correlation length, $(\xi_x + \xi_z)/2$, is on the order of 5 µm, somewhat independent of shear rate. The analogous projections of $S(\mathbf{q})$
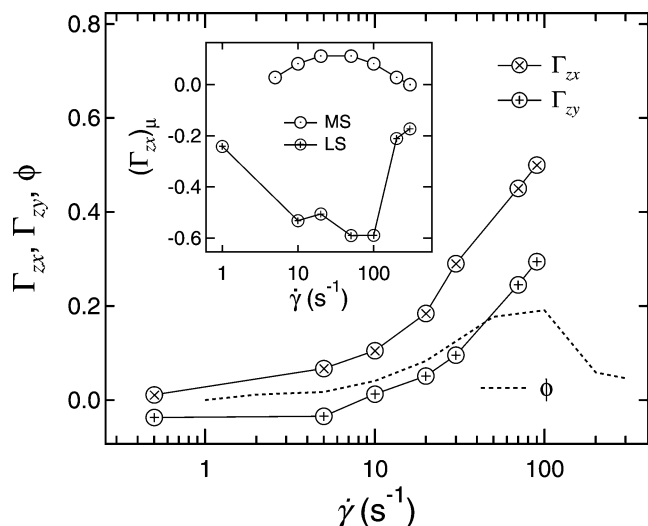
Fig. 12. The measured microstructural (SANS) [14] anisotropy factors Γ_{zx} and Γ_{zy} as a function of $\dot{\gamma}$ for the sample depicted in Figs. 10 and 11 (PEO2–LRD3). The lower curve is the volume fraction of macrodomains, $\phi(\dot{\gamma})$, deduced from the measured turbidity. The inset shows the optical anisotropy factors, $(\Gamma_{xz})_\mu$, obtained from both real-space optical data and small-angle light scattering, where the difference in sign reflects the inverted nature of the response in reciprocal space. Slightly negative values of Γ_{zy} at low $\dot{\gamma}$ are artifacts of curvature in the SANS shear cell.

(inset, Fig. 11) along both the flow (x) and vorticity (z) direction show a transition from a power-law exponent of -2 to -4, suggesting the presence of sharp interfaces.

The complete mesoscale structure is depicted in Fig. 12. The SANS anisotropy parameter obtained from our previously published data [14] can be defined as $\Gamma_{ij} = [S(q_0\hat{x}_i) - S(q_0\hat{x}_j)]/[S(q_0\hat{x}_i) + S(q_0\hat{x}_j)]$ ($i, j = z, x$ or z, y), where $q_0 \approx 0.08$ nm^{-1} is the equilibrium spacing between platelets deduced from SANS [14], $d = 2\pi/q_0 \approx 80$ nm. Over larger length scales, the optical anisotropy parameter can be defined as $(\Gamma_{zx})_\mu = (\xi_z - \xi_x)/(\xi_z + \xi_x)$ (in real-space) or $[S(q_c\hat{z}) - S(q_c\hat{x})]/[S(q_c\hat{z}) + S(q_c\hat{x})]$ (in reciprocal-space), where the wavevector q_c is taken as 1 μm^{-1}. The turbidity provides a measure of the average volume fraction of the segregated phase [24], $\phi(\dot{\gamma})$, which exhibits a maximum of around 0.20 in the vicinity of 100 s^{-1}. The microstructural (SANS) anisotropy becomes quite developed in both planes as macroscopic phase separation proceeds. Initially, the macrostructure (inset) exhibits modest elongation along the vorticity axis, but becomes more isotropic with decreasing turbidity at high $\dot{\gamma}$. A cartoon of the shear-induced mesostructure, spanning 5 decades in length scale, is shown as an inset in Fig. 11. In general, the gellike domains feel a viscous shear stress, σ_{xy}, and an internal elastic stress, τ_e, where τ_e acts tangentially along closed internal streamlines in the x–y plane [25]. We suggest that the 'biaxial' nature of the total stress in the x–y plane might induce an orientation with $\hat{n}$ parallel to the z-axis, although more detailed computational work would be needed to validate this somewhat intuitive physical picture.

4. Conclusions

We suggest that the response of the PEO2–LRD3 suspension can be qualitatively understood in terms of a critical shear rate, $\dot{\gamma}_c$. For $\dot{\gamma} < \dot{\gamma}_c$, the shear-induced reorientation of clay platelets is sufficiently slow that the polymer chains have time to diffuse in a manner that accommodates yielding of the orientational glass [15,19], and η thus resembles the viscosity of the pure clay. For $\dot{\gamma} > \dot{\gamma}_c$, however, the platelets move faster than the polymer can diffuse, fragmenting the quiescent network into macroscopic domains, leading to viscosity enhancement at high shear rates. Note that the characteristic lifetime of the reversible polymer–clay attractive interaction is much faster than the time scales of relevance here [14]. An expression for $\dot{\gamma}_c$ can be derived by equating the time required for a platelet to translate the distance d in response to the flow with the time required for the polymer to diffuse the same distance. Assuming Stokes–Einstein diffusion, this yields $\dot{\gamma}_c \approx 2k_BT/6\pi\eta R_g d^2$. Taking η as the viscosity of the pure (2%) polymer solution (which comprises the material between platelets) gives $\dot{\gamma}_c \approx 5$ s^{-1}, in excellent accord with the data. Upon cessation of shear, the domains quickly disappear and the samples become transparent, consistent with a timescale for "healing" on the order of $\dot{\gamma}_c^{-1} \approx 0.2$ s. It takes much longer, however, for the low-$\dot{\gamma}$ rheological response to recover.

It is interesting to note that the orientation observed here is quite different from that observed in other polymer–clay nanocomposites subjected to shear stress. The effect of shear on orientation in polymer–clay nanocomposites has been previously studied by a number of groups, and in some cases the full three-dimensional (3D) orientation of the polymer and clay has been determined [26–34]. In the conventional nomenclature, the two-dimensional clay platelets can align in three possible orientations under shear flow, often referred to as 'a', 'b', and 'c' [26]. In the perpendicular ('a') orientation, the surface normal aligns parallel to the vorticity (z) direction and the platelets lie in the plane of flow (x) and shear-gradient (y); in the transverse ('b') orientation, the surface normal aligns parallel to the flow (x) direction and the platelets lie in the plane of vorticity (z) and shear-gradient (y); and in the parallel ('c') orientation, the surface normal aligns parallel to the shear-gradient (y) direction and the platelets lie in the plane of flow (x) and vorticity (z).

The general or intuitive shear response of a nanoclay platelet in a polymer matrix is the 'c' orientation. This has been described by earlier studies on Nylon–clay nanocomposites [26]. Studies using in situ X-ray diffraction provide direct evidence for rheology-microstructure linkages in polypropylene nanocomposites [33]. Recent transmission electron microscopy (TEM) analysis suggests a house of cards structure in polypropylene–clay nanocomposite melts under elongational flow [34]. Strong strain-induced hardening and rheopexy features at higher deformation originate from a perpendicular alignment of the silicate to the stretching direction ('b' orientation). Although TEM is not an in

situ technique, it did reveal differences in the shear-flow versus elongational induced internal structure of the nanocomposite melt. These nanocomposites have strong interactions between the polymer matrix and the silicate layers. In the solutions described here, we observed the somewhat unusual and unexpected 'a' orientation, which we attribute to effects associated with macroscopic phase separation.

We note that when the viscosity data shown in Fig. 3a are recast as shear stress vs shear rate (Fig. 3b), no stress plateau is observed with the formation of domains, suggesting that although such a plateau might be associated with macroscopic phase separation within the context of shear banding transitions [23,35,36], it is not universal to biphasic effects in shear flow. We have suggested that the butterfly patterns that appear in sheared viscoelastic fluids can be understood within a single universal framework that is intimately linked to the elasticity of the dispersed or cluster phase [37]. We note that this interpretation is completely consistent with the behavior reported in Refs. [21] and [22], although its relationship to more well-studied rheological phenomena like shear banding is a point of continued research [23].

Also of note is the behavior of the first normal stress difference measured for PEO2–LRD3. The negative value under weak-to-modest shear correlates with the region of yielding for $\dot{\gamma} < \dot{\gamma}_c$, and we note that negative first normal stress differences have been associated with director tumbling in liquid-crystalline polymer melts [38]. It seems quite plausible, then, that the negative value of N_1 observed here reflects a 'tumbling' or continuous reorientation of the platelets. This idea would seem to be further supported by the observation that N_1 becomes positive in the vicinity of $\dot{\gamma}_c$, where domain interfaces first start to appear and yielding of the platelets starts to cease. We hope that the work described here will offer valuable physical insight into the broader phenomenon of shear-induced structure in polymer–clay nanocomposites and help guide the development of rigorous theoretical models of flow-induced orientation in these remarkably complex systems.

Acknowledgments

References

[1] Y. Kojima, A. Usuki, M. Kawasumi, A. Okada, Y. Fukushima, T. Kurauchi, O. Kamigaito, J. Mater. Res. 8 (1993) 1185.
[2] R. Chapman, P. Mulvaney, Chem. Phys. Lett. 349 (2001) 358.
[3] O. Wilson, G.J. Wilson, P. Mulvaney, Adv. Mater. 14 (2002) 1000.
[4] P.J. Yoon, T.D. Fornes, D.R. Paul, Polymer 43 (2002) 6727.
[5] E.P. Giannelis, R. Krishnamoorti, E. Manias, Adv. Polym. Sci. 138 (1999) 107.
[6] S.D. Burnside, E.P. Giannelis, Chem. Mater. 7 (1995) 1597.
[7] S.D. Burnside, E.P. Giannelis, J. Polym. Sci. Polym. Phys. 38 (2000) 1595.
[8] D.C. Lee, L.W. Jang, J. Appl. Polym. Sci. 68 (1998) 1997.
[9] P.F. Luckham, S. Rossi, Adv. Colloid Interface Sci. 82 (1992) 43.
[10] S.D. Burnside, H.C. Wang, E.P. Giannelis, Chem. Mater. 11 (1999) 1055.
[11] J. Gabriel, F. Camerel, B.J. Lemaire, H. Desvaux, P. Davidson, P. Batail, Nature 413 (2001) 504.
[12] G. Schmidt, A.I. Nakatani, C.C. Han, Rheol. Acta 41 (2002) 45.
[13] J. Swenson, M.V. Smalley, H.L.M. Hatharasinghe, G. Fragneto, Langmuir 17 (2001) 3813.
[14] G. Schmidt, A.I. Nakatani, P.D. Butler, A. Karim, C.C. Han, Macromolecules 33 (2000) 7219;
G. Schmidt, A.I. Nakatani, P.D. Butler, C.C. Han, Macromolecules 35 (2002) 4725.
[15] M. Kroon, W.L. Vos, G.H. Wegdam, Phys. Rev. E 57 (1998) 1962.
[16] J.D. Ramsay, S.W. Swanton, J. Bunce, J. Chem. Soc. Faraday Trans. 86 (1990) 3919.
[17] S. Lin-Gibson, G. Schmidt, H. Kim, C.C. Han, E.K. Hobbie, J. Chem. Phys. 119 (2003) 8080.
[18] S. Kim, J. Yu, C.C. Han, Rev. Sci. Instrum. 67 (1996) 3940.
[19] See, for example, F. Pignon, A. Magnin, J.-M. Piau, B. Cabane, P. Lindner, O. Diat, Phys. Rev. E 56 (1997) 3281, and references therein.
[20] The field $\psi(\mathbf{r}) = 1$ or 0 if $\mathbf{r}$ falls inside or outside a domain, respectively. For a discussion of the link between this spatial pattern and the viscoelasticity of the dispersed phase, as well as details of the procedure used to extract the field $\psi(\mathbf{r})$ from the micrographs, see E.K. Hobbie, et al., J. Chem. Phys. 117 (2002) 6350.
[21] J.V. Degroot, C.W. Macosko, T. Kume, T. Hashimoto, J. Colloid Interface Sci. 166 (1994) 404.
[22] P. Varadan, M.J. Solomon, Langmuir 17 (2001) 2918.
[23] J. Vermant, Curr. Opin. Colloid Interface Sci. 6 (2001) 489.
[24] See, for example, M. Kerker, The Scattering of Light and other Electromagnetic Radiation, Academic Press, London, 1969. For soft domains, we assume that turbidity scales linearly with ϕ in the semidilute regime, where the constant of proportionality is obtained by assuming that the optimum threshold level at the highest turbidity gives an accurate measure of true area fraction in the micrographs, which is then used to estimate volume fraction. The micrographs are thus thresholded in a manner that is consistent with the measured turbidity.
[25] For a discussion of τ_e and its relation to droplet shape and internal droplet stress, see E.K. Hobbie, K.B. Migler, Phys. Rev. Lett. 82 (1999) 5393;
F. Migrhi, M.A. Huneault, J. Rheol. 45 (2001) 783.
[26] R. Krishnamoorti, K. Yurekli, Curr. Opin. Colloid Interface Sci. 6 (2001) 464.
[27] H. Fong, W.D. Liu, C.S. Wang, R.A. Vaia, Polymer 43 (2002) 774.
[28] G. Jimenez, N. Ogata, H. Kawai, T. Ogihara, J. Appl. Polym. Sci. 64 (1997) 2211.
[29] N. Ogata, G. Jimenez, H. Kawai, T. Ogihara, J. Polym. Sci. Polym. Phys. 35 (1997) 389.
[30] Y. Kojima, A. Usuki, M. Kawasumi, A. Okada, T. Kurauchi, O. Kamigaito, K. Kaji, J. Polym. Sci. Polym. Phys. 32 (1994) 625.
[31] A. Bafna, G. Beaucage, F. Mirabella, S. Mehta, Polymer 44 (2003) 1103.

[32] K. Varlot, E. Reynaud, M. Kloppfer, G. Vigier, J. Varlet, J. Polym. Sci. Polym. Phys. 39 (2001) 1360.

[33] A. Lele, M. Mackley, G. Galgali, C. Ramesh, J. Rheol. 46 (2002) 1091.

[34] M. Okamoto, P.H. Nam, P. Maiti, T. Kotaka, N. Hasegawa, A. Usuki, Nano Lett. 1 (2001) 295.

[35] J.-F. Berret, D.C. Roux, P. Lindner, Eur. Phys. J. B 5 (1998) 67.

[36] See, for example, P.D. Olmsted, C.-Y.D. Lu, Phys. Rev. E 56 (1997) R55, and references therein.

[37] E.K. Hobbie et al., Phys. Rev. E, submitted.

[38] See, for example, R.G. Larson, The Structure and Rheology of Complex Fluids, Oxford Univ. Press, New York, 1999, and references therein.